Earth and Planetary Science Letters 445 (2016) 92–103

Contents lists available at ScienceDirect

Earth and Planetary Science Letters

www.elsevier.com/locate/epsl

Viscous anisotropy of textured olivine aggregates, Part 1: Measurement of the magnitude and evolution of anisotropy

Lars N. Hansen [a,*], Jessica M. Warren [b], Mark E. Zimmerman [c], David L. Kohlstedt [c]

[a] Department of Earth Sciences, University of Oxford, UK
[b] Department of Geological Sciences, University of Delaware, DE, USA
[c] Department of Earth Sciences, University of Minnesota, MN, USA

ARTICLE INFO

Article history:
Received 29 November 2015
Received in revised form 30 March 2016
Accepted 7 April 2016
Available online 22 April 2016
Editor: J. Brodholt

Keywords:
viscous anisotropy
olivine microstructure
crystallographic preferred orientation
texture evolution

ABSTRACT

The development of crystallographic textures in olivine-rich rocks leads to a marked anisotropy in viscosity of the upper mantle, strongly influencing a variety of large-scale geodynamic processes. Most estimates of the magnitude of viscous anisotropy in the upper mantle are derived from micromechanical models that predict textural and mechanical evolution numerically. Unfortunately, relatively few data exist with which to benchmark these models, and therefore their applicability to geodynamic processes remains in question. Here we present the results from a series of laboratory deformation experiments that yield insight into the magnitude and evolution of the anisotropy of olivine aggregates during deformation along complex loading paths. Aggregates of Fo_{50} olivine were first deformed in extension in a gas-medium apparatus at a temperature of 1473 K, confining pressure of 300 MPa, and a variety of stresses and strain rates. Early in the extension experiments, samples exhibited viscosities similar to those previously determined for isotropic aggregates. Extensional deformation was accompanied by formation of crystallographic textures with [100] axes dominantly aligned with the extension axis. Samples were subsequently deformed in torsion under similar conditions to shear strains of up to 15.5. Early in the torsion experiments, samples supported stresses a factor of ~2 larger than measured at the end of extension experiments, demonstrating a marked anisotropy in viscosity. Textures at the end of torsion experiments exhibited [100] axes dominantly aligned with the shear direction, comparable to previous experimental observations. Evolution of the textures resulting from extension to those resulting from torsion was analyzed through examination of radial sections of torsion samples. Our results confirm that texture produces viscous anisotropy in olivine aggregates, and we provide a simple, calibrated parameterization of viscous anisotropy for use in geodynamic models. Our results also provide an extensive dataset for future calibration of micromechanical models that track the evolution of anisotropy in upper mantle rocks.

1. Introduction

Many large-scale phenomena in the solid Earth depend directly on the viscosity of upper-mantle rocks. Notably, spatial and temporal variability in the viscosity of mantle rocks dramatically influences a number of key processes including localization of deformation into tectonic plate boundaries (e.g., Bercovici et al., 2000; Tackley, 2000), evolution and structure of mantle flow (e.g., Lenardic et al., 2003), flexure of the lithosphere in response to loading from ice sheets or other masses (e.g., Mitrovica and Forte, 2004), and viscoelastic relaxation of stresses after seismic events (e.g., Freed et al., 2012).

Heterogeneity in the spatial and temporal distributions of upper-mantle viscosity results from the evolution of thermodynamic, chemical, and microstructural conditions. For instance, laboratory-based investigations have demonstrated that the viscosity of olivine aggregates depends on temperature, pressure, water fugacity, oxygen fugacity, melt fraction, melt distribution, and grain size (e.g., Hirth and Kohlstedt, 1995; Mei and Kohlstedt, 2000; Keefner et al., 2011; Raterron et al., 2012). In addition to these relatively well-studied state variables, aggregates in which crys-

* Corresponding author.
E-mail addresses: lars.hansen@earth.ox.ac.uk (L.N. Hansen), warrenj@udel.edu (J.M. Warren), zimme030@umn.edu (M.E. Zimmerman), dlkohl@umn.edu (D.L. Kohlstedt).

http://dx.doi.org/10.1016/j.epsl.2016.04.008

tals exhibit preferred crystallographic orientations should exhibit anisotropy in their viscosity, because crystallographic alignment inherently imparts anisotropy to bulk material properties Only very recently have experiments demonstrated that crystallographic textures significantly affect the viscosity of olivine aggregates (Hansen et al., 2012a, 2012c). Thus, heterogeneity in the viscosity of mantle rocks can additionally arise either from variation in the strength of a texture or from variation in the orientation of the texture relative to that of the applied stress.

The role of viscous anisotropy in the flow of the upper mantle has been examined theoretically in a number of studies. Numerical simulations have demonstrated that viscous anisotropy in the upper mantle affects the boundary layer thickness of convection cells (Christensen, 1987), modifies the thermal evolution of the lithosphere (Hearn et al., 1997), offsets geophysical signals from mass anomalies during post-glacial rebound (Christensen, 1987), influences the horizontal component of ice sheet motion (Han and Wahr, 1997), modifies the temporal and spatial distributions of density instabilities leading to drips forming from a dense lithosphere (Lev and Hager, 2008), and modifies the thermal structure above subducting slabs (Lev and Hager, 2011). Tommasi et al. (2009) demonstrated through numerical simulation that spatial heterogeneities in crystallographic fabric can lead to the formation of large-scale shear zones. This suggestion is supported by field studies illustrating that major tectonic fabrics observed at outcrop and mountain belt scales tend to parallel the underlying upper-mantle fabric revealed by the anisotropy of seismic wave propagation (e.g., Vauchez et al., 1998. Detailed microstructural investigations of exhumed mantle shear zones also indicate that viscous anisotropy associated with texture formation plays a role in shear zone initiation (Michibayashi and Mainprice, 2004; Skemer et al., 2013).

Currently, most estimates of the viscous anisotropy of mantle rocks are derived from micromechanical simulations of olivine deformation (e.g., Tommasi et al., 2009). The main input into these simulations is the relative ease of activation of potential slip systems in olivine, which is primarily determined from deformation experiments on single crystals of olivine (Durham et al., 1977; Bai et al., 1991). There are, however, relatively few results from deformation experiments on anisotropic aggregates with which to benchmark these micromechanical models. Previous studies have investigated only a limited range of deformation paths (e.g., Wendt et al., 1998; Hansen et al., 2012a, 2012c; Boneh and Skemer, 2014). In addition, these studies do not give insight into the time evolution of viscous anisotropy after a change in the kinematic conditions, a critical aspect of complex flow in the upper mantle (e.g., Castelnau et al., 2009).

To address the lack of laboratory data for calibration of micromechanical models that would allow viscous anisotropy to be incorporated into a wide range of geodynamic simulations, we have conducted a series of deformation experiments. In this contribution, we describe laboratory experiments in which olivine aggregates are initially deformed in extension and subsequently deformed in torsion. The experiments yield microstructural data that illustrate the evolution of texture strength, orientation, and symmetry in response to a change in deformation geometry. The experiments also yield mechanical data that demonstrate the manner in which viscosity varies as a function of textural characteristics and orientation of the principal stresses relative to the texture. In a subsequent contribution, we use these data to calibrate a new set of micromechanical models for easy incorporation into geodynamic simulations.

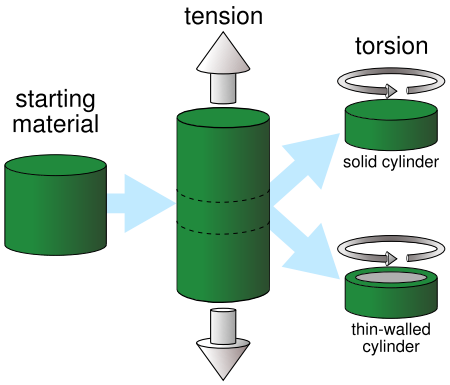

Fig. 1. Overview of experimental design. Hot-pressed aggregates of olivine (green) were deformed in extension. Short cylinders prepared from samples deformed in extension were subsequently deformed in torsion as either solid cylinders or thin-walled cylinders with the central region replaced with a Ni plug (gray). (For interpretation of the references to color in this figure legend, the reader is referred to the web version of this article.)

2. Methods

2.1. Sample preparation

Aggregates of Fo_{50} were fabricated following the methods outlined in several previous studies (Zhao et al., 2009; Hansen et al., 2012b, 2012c, 2014). Fo_{50} (rather than Fo_{90}) was used because of its fast grain-growth kinetics, which facilitates synthesis of coarse-grained starting materials, and for its low strength relative to San Carlos olivine (Fo_{90}), which reduces the likelihood of slip at piston-sample interfaces during torsion experiments. First, fayalite powders were initially synthesized by reacting fine-grained mixtures of Fe_2O_3 and SiO_2 in a gas-mixing furnace at 1410 K for 100 h with a mixture of CO and CO_2 specified to control the oxygen partial pressure at $P_{O_2} \approx 10^{-7}$ Pa. Then, this fayalite powder was reground and mixed with San Carlos olivine powder in a ratio suitable to produce equal amounts of Fe and Mg. Finally, this mixture of powders was reacted at 1673 K for 40 h in an one-atmosphere furnace filled with CO plus CO_2 in a ratio specified to control the oxygen partial pressure at $P_{O_2} \approx 10^{-4}$ Pa. This calcination process also removes any dissolved water initially present in the San Carlos olivine powders.

Aggregates of olivine used in deformation experiments were prepared from the Fo_{50} powders. Powders were first uniaxially pressed into cylindrical Ni cans with a pressure of 100 MPa at room temperature. The Ni cans were capped with Ni discs and isostatically hot-pressed in an internally heated gas-medium apparatus (Paterson, 1990) at the University of Minnesota. Hot pressing was conducted at a temperature of 1473 K and confining pressure of 300 MPa for 5 to 8 h. During hot pressing, aggregates densified to $<1\%$ porosity and experienced significant grain growth. Scanning electron microscopy observations of hot-pressed samples reveal no evidence for residual glass after sintering. The ends of the cylinders of hot-pressed aggregates were subsequently ground to yield right cylinders approximately 10 mm in diameter and 20 mm in length.

2.2. Deformation experiments

We performed extension experiments followed by torsion experiments; this order is reversed from that used in our previous experiments (Hansen et al., 2012a). As depicted in Fig. 1, textured aggregates were initially created during extension experiments (PT0715 and PT0750) to provide material for subsequent torsion tests. Each sample deformed in extension was sectioned to

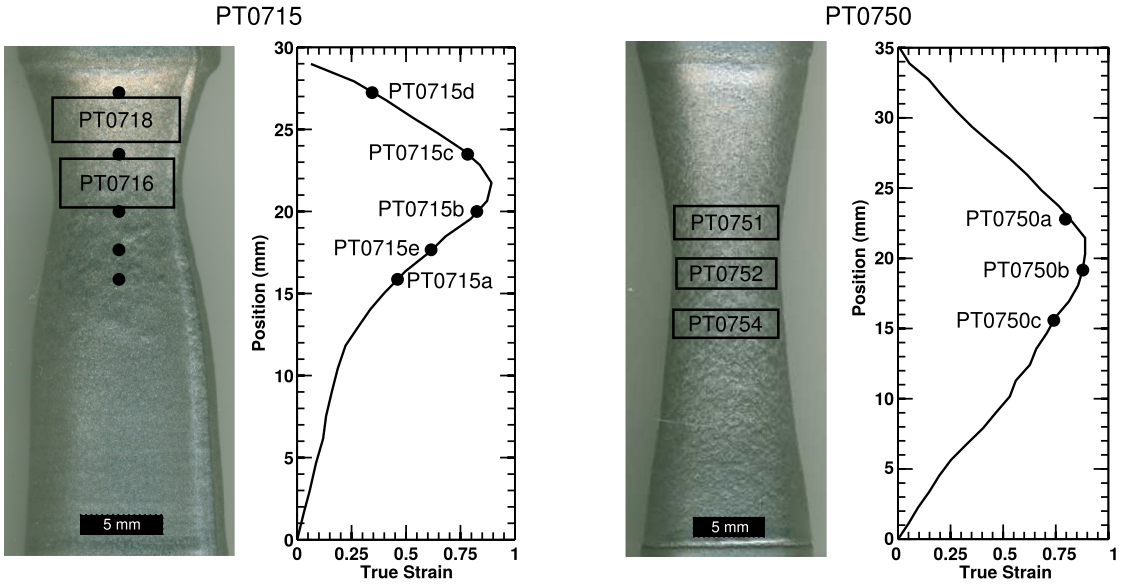

Fig. 2. Variation of strain along the length of samples deformed in extension and locations of samples used in torsion experiments. Samples deformed in extension are shown in their Fe jackets; note that the spatial scale is different between the two assemblies. Strain was calculated as a function of position from the local sample diameter. Rectangles denote the regions from which cylinders were extracted for torsion experiments. Solid circles denote the regions from which material was extracted for microstructural analysis. The central cores of samples extracted from PT0750 were used for microstructural analysis (PT0750a, b, and c).

derive multiple samples for torsion experiments. Short solid cylinders from PT0715 were used for torsion tests PT0716 and PT0718 (Fig. 2). Short cylinders from PT0750 were cored and used for thin-walled torsion experiments PT0751, PT0752 and PT0754 (Fig. 2).

For the extension experiments, hot-pressed aggregates still jacketed in Ni were stacked between dense alumina and zirconia pistons and inserted into an Fe jacket. Jacketed assemblies were then inserted into the same gas apparatus used for hot pressing. The internal furnace was used to heat the samples to 1473 K. Temperature at the sample was maintained to ±2 K for the duration of the experiment. The gas pressure was increased to 300 MPa and maintained to ±1 MPa for the duration of the experiment. Extension tests were conducted by moving the actuator at a constant displacement rate. Displacements and loads were measured internal to the pressure vessel and therefore not subject to corrections due to friction on o-ring seals. In experiment PT0750, a constant displacement rate was maintained throughout the experiment. In experiment PT0715, constant displacement rates were maintained for fixed intervals, between which the rate was increased to perform displacement rate-stepping tests. For each change in displacement rate, the new rate was held until a steady-state extensional load was reached, after which the rate was returned to the original controlling rate until a steady-state load was again attained.

Extension experiments were continued to a maximum true strain, ln(final length/initial length), of ∼0.56, assuming homogeneous deformation. With increasing strain, samples became longer and thinner, maintaining constant volume. For a fixed load and displacement rate, the increased length results in a decrease in strain rate, and the decreased cross-sectional area results in an increase in stress. For data collected at low strains (<14%), both of these effects were accounted for by assuming that the deformation was homogeneously distributed throughout the sample. By the end of the experiment, samples exhibited non-uniform strain. After each extension experiment, the sample assembly was imaged with a desktop scanner to characterize the non-uniformity of sample thinning. Images of sample assemblies after deformation in extension are provided in Fig. 2. Because plastic deformation is a constant volume process, the diameter of the sample can be directly related to the local strain. The local true axial strain, ε, is related to the local diameter, w, and the initial diameter, w_i, through the relationship

$$\varepsilon = \ln\left(\frac{w_i}{w}\right)^2. \quad (1)$$

Calculated values of local true strain are depicted as a function of position along the sample assemblies in Fig. 2b. We also calculated the local stress at the end of the test using the measured load and local diameter. Local strain rates were calculated assuming that variations in strain rate along the length of the sample were proportional to the variations in strain, which are depicted in Fig. 2.

Samples deformed in extension were sectioned into discs for microstructural analysis and torsion testing (Fig. 1). Discs with heights of 2.5 to 3.9 mm and diameters of 5.4 to 6.4 mm were extracted from the locations indicated by boxes in Fig. 2 for subsequent torsion experiments. For microstructural analysis of sample PT0715, thin discs (<2 mm thick) were extracted from the location of the black dots in Fig. 2 (PT0715a–e). For sample PT0750, discs extracted for torsion experiments were cored with a 3.3-mm outer-diameter diamond coring drill, and the cores were retained for microstructural analysis (PT0750a–c).

For torsion experiments, extracted discs, still jacketed in Fe and Ni, were stacked between porous alumina, dense alumina, and zirconia pistons and inserted into a new Fe jacket. A Ni plug was placed in the center of thin-walled cylinders extracted from PT0750 (Fig. 1). Jacketed assemblies were then reinserted into the gas apparatus and again brought to a temperature of 1473 K and confining pressure of 300 MPa. Samples were deformed at a constant twist rate. The twist was measured external to the pressure vessel, and the torque was measured internal to the pressure vessel. Stresses were calculated following the approach described by Paterson and Olgaard (2000) for solid and thin-walled cylinders using a stress exponent of $n = 4.1$ (Hansen et al., 2012c) and the operation of a single deformation mechanism. These assumptions introduce a small error (<10%) for a thin-walled cylinder for which the stress is nearly constant along its radius. A solid cylinder experiences a more substantial variation in stress along its radius; calculated stresses and strain rates correspond to the material at the outermost radius and are, therefore, the maximum experienced by the sample.

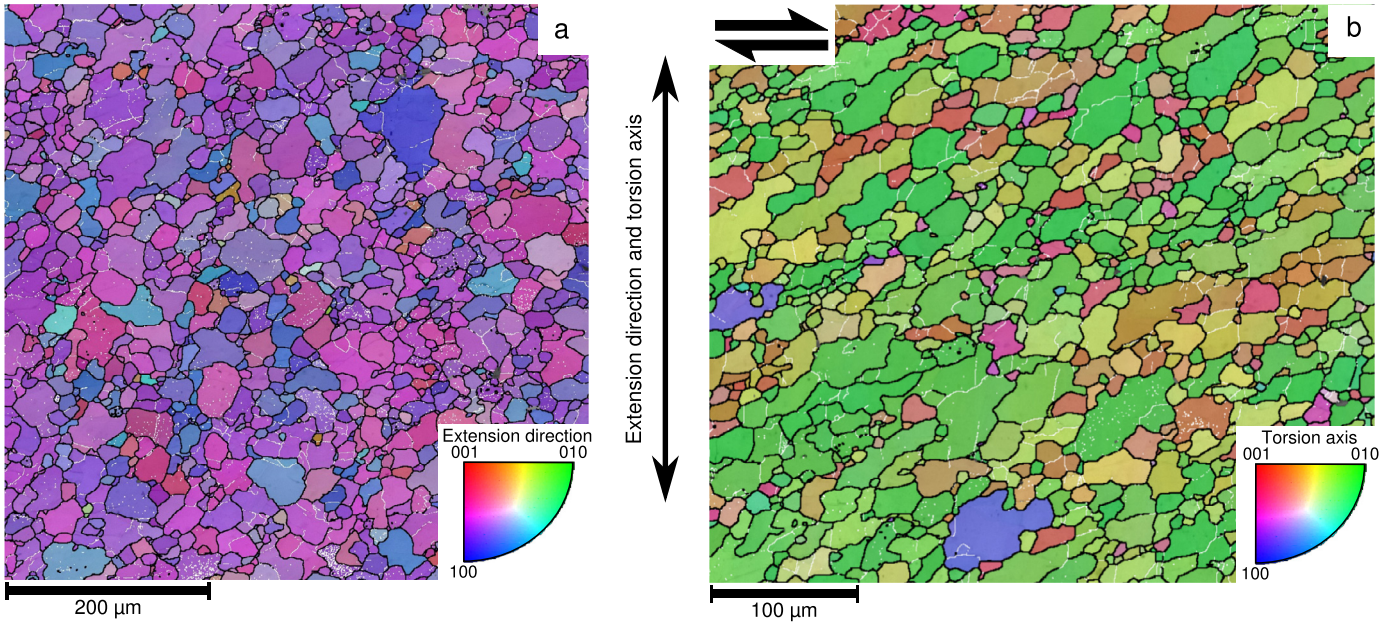

Fig. 3. Orientation maps constructed from EBSD data from samples deformed in (a) extension (PT0750c) and (b) torsion (PT0754), where PT0750c represents the starting material for PT0754. Olivine crystallographic orientation is colored relative to the direction of the applied extensional load in (a) and to the direction of the torsion axis (i.e., vertical axis normal to the shear plane) in (b). This coloring is superimposed over a gray scale map of Kikuchi band contrast, with lighter shades reflecting higher quality EBSD patterns. Grain boundaries (misorientations $>10°$) are denoted by black lines. Subgrain boundaries with misorientations between 1.5 and 10° are denoted by white lines.

A correction to the torque was applied based on the strength of the Ni and Fe jackets and the Ni central cylinder, as outlined by Hansen et al. (2012b). Torque corrections were typically 1 to 5% of the total torque. The twist rate was maintained constant throughout the experiments, except for PT0716 for which twist rate-stepping tests were conducted. For each change in twist rate, the new rate was held until a steady-state torque was reached, after which the rate was returned to the original controlling rate until a steady-state torque was again achieved. Because samples used for torsion in this study were a factor of ~2 smaller in diameter than typical for experiments in our apparatus, torques were a factor of ~4 smaller than required to deform larger diameter samples. As a result, the ratio of signal to mechanical noise is significantly larger than in our previous torsion studies on the same material (e.g., Hansen et al., 2012c). Mechanical noise is generally manifested as an oscillating signal with a period in twist of $\sim 2\pi$ radians and, therefore, attributed to off-axis loading of the sample column. Even though we applied a filter to remove signals with a period near 2π radians, substantial scatter in our data remains.

2.3. Microstructural analysis

Microstructural analyses were performed on samples prior to extension experiments, between extension experiments and torsion experiments, and after torsions experiments. Samples were polished as thick sections with the section parallel to the extension axis or the torsion axis. For samples deformed in torsion, sections were cut (i) either along a radial section such that the shear direction was into/out of the plane of the section or (ii) along a tangential section as close to the outer radius as possible such that the shear direction was in the plane of the section. Sections were polished with SiC and diamond lapping films of increasingly finer grit size down to 0.5 μm. Sections were then polished with colloidal silica with a grit size of either 0.02 or 0.04 μm for up to 60 min.

Microstructures in polished sections were analyzed using electron-backscatter diffraction (EBSD) in a scanning electron microscope. We employed an FEI Quanta 200 with a W filament housed at Stanford University and outfitted with an Oxford Instruments Nordlys F + EBSD detector and the AZtec software package. The electron beam was rastered across the sample using step sizes of 0.2 to 0.5 μm, and the crystallographic orientation at each point was determined (Fig. 3). EBSD data were post-processed using the Channel5 software package. Isolated pixels with large misorientations relative to neighboring pixels were considered to be misindexed and therefore were removed from the data set. Pixels for which an orientation solution was not identified were assigned the average orientation of neighboring pixels if at least 8 nearest neighbor pixels did have solutions. This procedure was repeated for pixels with only 7 nearest neighbors with solutions and again for those with only 6 nearest neighbors with solutions. Orientation and grain-boundary maps were constructed assuming a minimum misorientation of 10° and 1.5° for grain boundaries and subgrain boundaries, respectively.

Microstructural data are presented in Table 1, and pole figures demonstrating the crystallographic textures are presented in Fig. 5. Pole figures were constructed for each data set by randomly selecting one point for each grain. At least 300 grains were included in each pole figure, and >700 grains were included in most pole figures from torsion experiments. A list of grain orientations was then exported from Channel5 and processed further with the MTEX toolbox for MATLAB™ (Bachmann et al., 2010). For each set of orientations, an orientation distribution function was determined using a kernel halfwidth of 10°. To visualize the texture, we display pole figures for [100], [010], and [001] of each grain plotted as a point colored by the value of the orientation distribution function for that orientation in Fig. 5. For radial sections of two torsion samples (PT0716 and PT0718), maps were made from the center to the outer edge of each sample (Fig. 5). Microstructural data were then sub-sampled with a 200-μm wide sliding window to quantify the microstructural evolution along the sample radius (Table S1, Supplemental Movie).

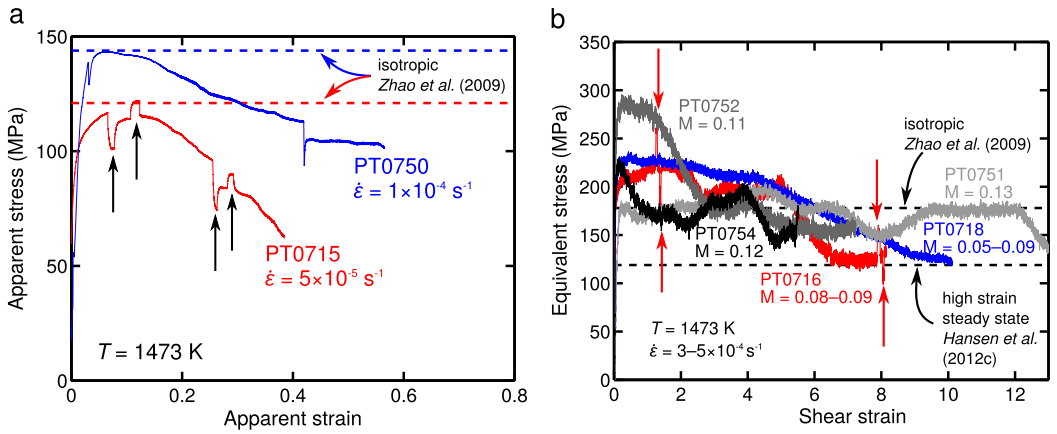

Fig. 4. Stress as a function of strain during (a) extension experiments and (b) torsion experiments. (a) Extension experiments were conducted at constant axial displacement rate, and torsion experiments were conducted at constant twist rate, resulting in constant shear strain rate at any given radius within each sample. The term "apparent" refers to the assumption that sample volume remained constant and that strain is uniformly distributed throughout the sample. The actual values of stress and strain varied both spatially and temporally due to changes in the diameter of each sample along its length. Values of extensional strain are calculated as ln(final length/original length). (b) The additional dashed line indicates the flow law for the steady-state stress obtained at the end of torsion experiments (Hansen et al., 2012c). Sample names are given along with the texture strength (M index) at the beginning of the torsion experiments. In both panels, dashed lines indicate the stress predicted for isotropic viscosity (Zhao et al., 2009); arrows denote points at which the strain rate was changed to determine the dependence of strain rate on stress. The increased noise in the stress measurements for torsion experiments relative to tension experiments results from the small sample size, and therefore small torques, in torsion experiments.

Table 1
Microstructural data from extension experiments and torsion experiments. As in Fig. 5, data from torsion experiments are aligned with data from corresponding samples deformed in extension. Data for PT0716 and PT0718 correspond to data from the high-strain domain.

Extension					Torsion				
Sample	True strain	M-index	J-index	Grain size (μm)	Sample	Shear strain	M-index	J-index	Grain size (μm)
PT0715a	0.46	0.05	1.7	18.3					
PT0715b	0.82	0.08	2.7	14.9	PT0716	8.2	0.42	13.8	12.9
PT0715c	0.78	0.09	2.6	14.0	PT0718	10.1	0.52	17.6	15.6
PT0715d	0.34	0.05	1.6	22.1					
PT0715e	0.61	0.06	1.6	20.4					
PT0750a	0.82	0.13	3.9	20.3	PT0751	15.5	0.37	14.0	14.6
PT0750b	0.88	0.11	4.1	21.3	PT0752	7.2	0.53	19.4	14.3
PT0750c	0.75	0.12	3.5	21.5	PT0754	5.5	0.40	11.8	20.4

3. Results

3.1. Microstructural results

A microstructure typical of those developed in extension tests is depicted in Fig. 3a. The average grain size is reduced from 27 μm in the starting material (Table 1) to between 14 and 22 μm after extension experiments (Table 1). Grain shapes do not exhibit a substantial asymmetry, and no systematic shape fabric is observed, as confirmed by image cross correlation (Heilbronner, 1992) of grain boundaries in the map in Fig. 3a. Subgrain development is common, especially in regions with larger grain sizes. Many grain boundaries exhibit significant local curvature, typical of microstructures in which significant grain-boundary migration has occurred (Urai et al., 1986). The polishing procedure introduces some relief to sample surfaces due to differential chemical etching of grain boundaries and of grains of differing orientations. A qualitative assessment of secondary-electron images reveals little change of the microstructure along the radius of samples deformed in extension.

A typical microstructure formed in the torsion experiments is presented in Fig. 3b. Grain sizes measured from tangential sections near the outer radius of torsion samples are reduced from 27 μm to between 13 and 20 μm (Table 1). Maximum shear strains in torsion samples range from 5.5 to 15.5; no significant microstructural evolution is observed over this strain interval. Grains have aspect ratios of roughly 2:1 with the long axis oriented ∼30° anticlockwise to the shear plane on average (Fig. 3b). Subgrain development is pervasive and, as in extension samples, many grain boundaries exhibit significant local curvature.

Crystallographic textures formed during the extension experiments are presented in Fig. 5. Distributions of [100] axes tend to form girdles describing small circles at ∼35° to the extension axis. Distributions of [010] axes form girdles normal to the extension axis. Distributions of [001] axes tend to form girdles describing small circles at ∼50° to the extension axis. The strengths of the crystallographic fabrics are moderate with values of the M-index and J-index ranging from 0.05 to 0.13 and 1.6 to 4.1, respectively (Table 1).

Crystallographic textures developed near the outer radius of torsion samples are also depicted in Fig. 5. The fabrics are very similar over the illustrated range in shear strain (5.5 to 15.5) and consistent with previous observations on olivine samples deformed to high strain (Bystricky et al., 2000; Hansen et al., 2012c, 2014). Textures are characterized by point maxima of [100] axes parallel to the shear direction, point maxima of [010] axes normal to the shear plane, and point maxima of [001] axes normal to the shear direction and within the shear plane. Both [010] and [001] axes exhibit weak girdling. Note that the poles to girdles of [001] axes are inclined by ∼10° to the shear direction. The crystallographic fabrics are strong, with values of the M-index and J-index ranging from 0.37 to 0.53 and 11.8 to 19.4, respectively (Table 1).

Radial sections were mapped in the two solid-cylinder samples (PT0716 and PT0718) initially deformed in extension and subsequently deformed in torsion. The orientation map from PT0716 presented in Fig. 6 demonstrates that grain orientations system-

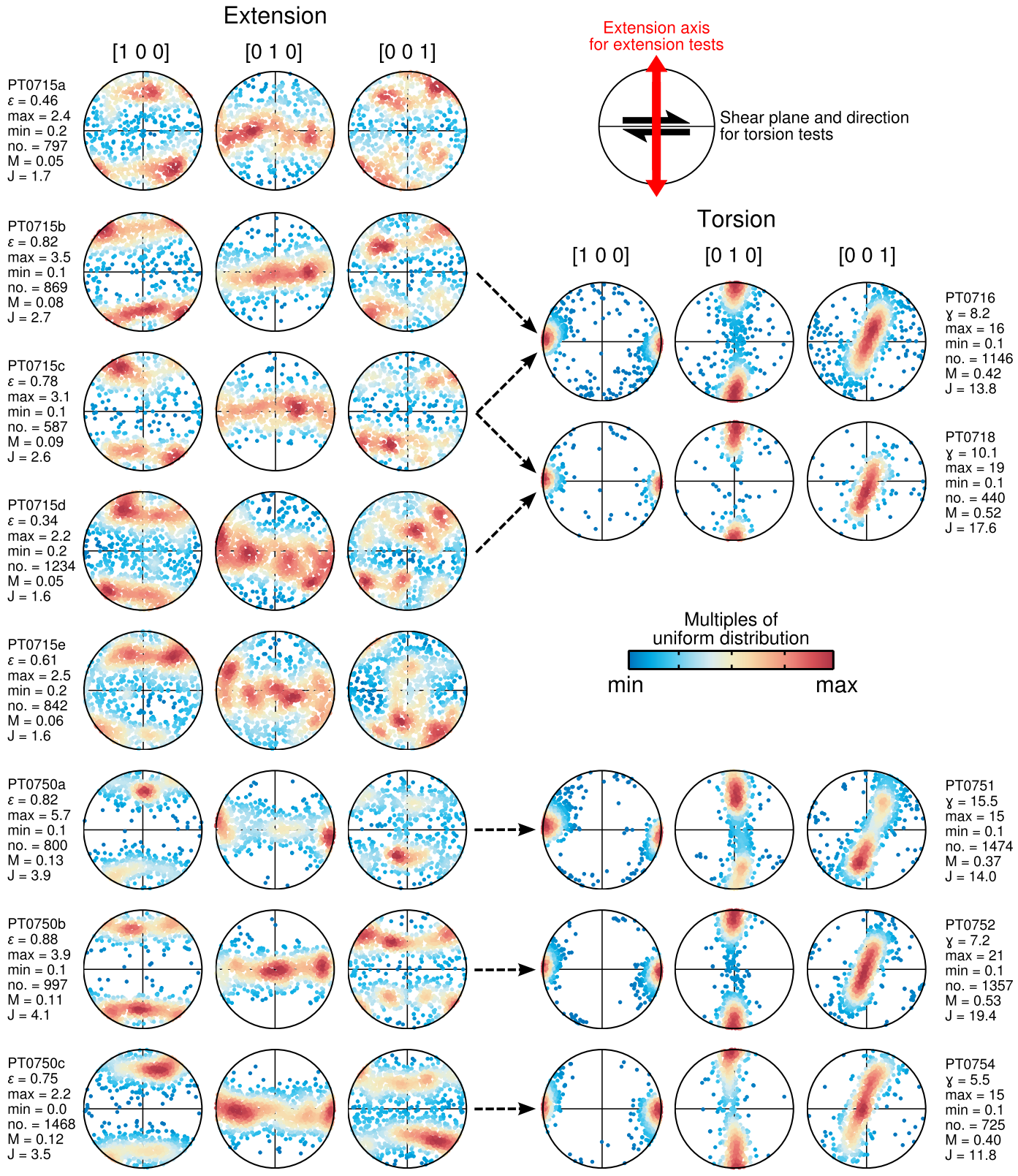

Fig. 5. Crystallographic orientation distributions for samples deformed in extension and samples deformed in torsion. Distributions are one point per grain plotted on equal-area lower-hemisphere projections. Data points are colored according to the value of the determined orientation distribution function, which is reported as multiples of a uniform distribution. True strain (ε) or shear strain (γ), number of grains (no.), M-index (M), and J-index (J) are given for each sample. Dashed arrows indicate which samples deformed in extension were used as starting material for torsion experiments.

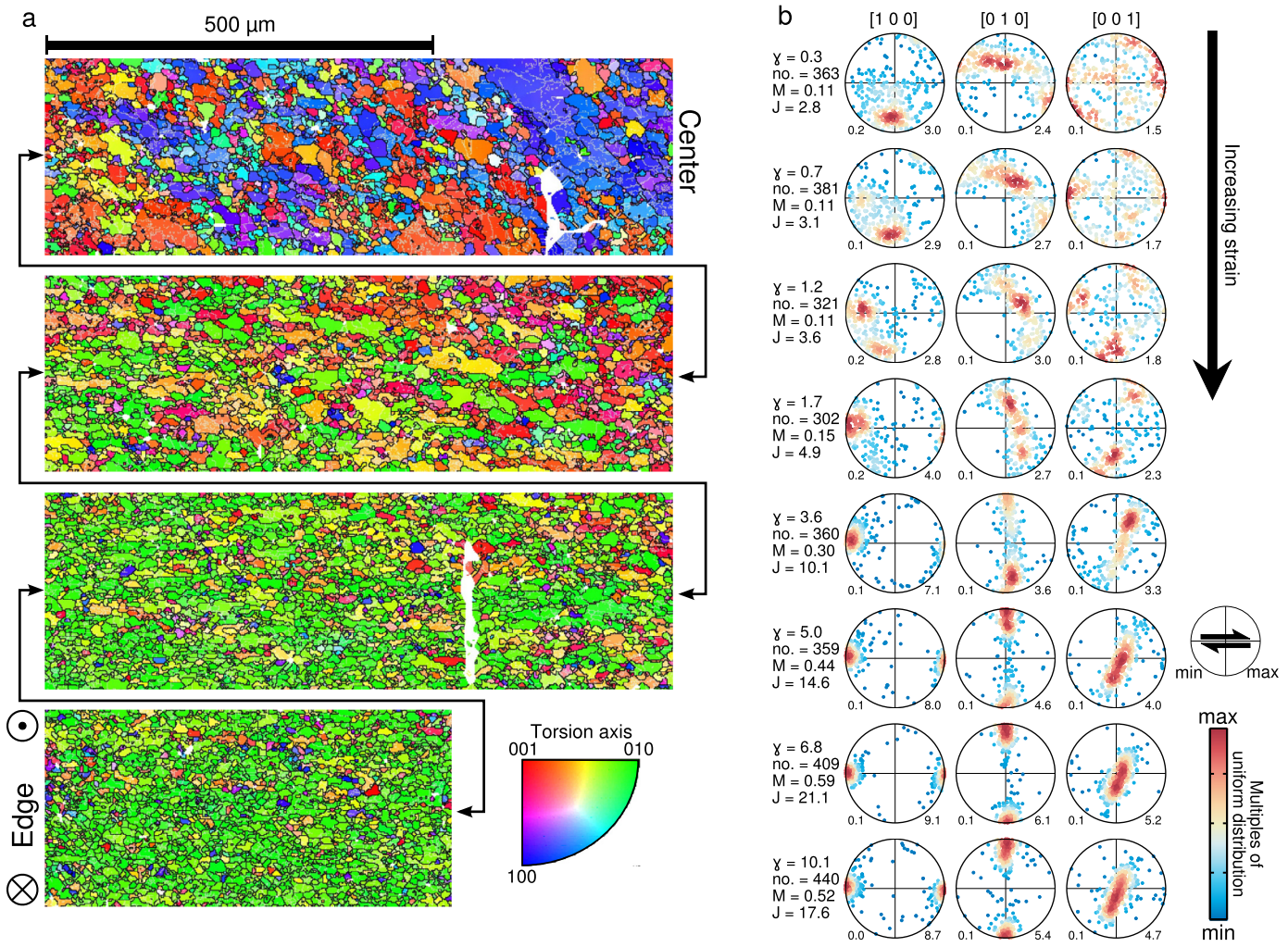

Fig. 6. Microstructures along axial sections of samples deformed in torsion constructed from EBSD data. (a) A single orientation map from sample PT0716 that extends continuously from the center to the outer radius of the sample. Olivine crystallographic orientation is colored according to the torsion axis (i.e., vertical). The shear sense is indicated by the arrow tip and tail. Grain boundaries (misorientations $>10°$) are denoted by black lines. Subgrain boundaries (misorientations $>1.5°$ and $<10°$) are denoted by white lines. (b) Crystallographic orientation distributions for the axial section profile of a sample deformed in torsion (PT0718), arranged in order of increasing strain (and increasing radius). Distributions are one point per grain plotted on equal-area lower-hemisphere projections. Data points are colored according to the value of the determined orientation distribution function reported in multiples of uniform distribution. Shear strain (γ), number of grains (no.), M-index (M), and J-index (J) are given for each sample. The observed microstructural evolution is consistent between PT0716 and PT0718.

atically evolve from near the center of the sample, where torsional strains are smallest, to the outer radius, where torsional strains are highest. Near the center of the sample the microstructure and orientation maps are similar to those observed in samples deformed in extension (Fig. 3a), whereas near the edge of the sample the microstructure and orientation maps are similar to those observed in tangential sections of other samples deformed in torsion (Fig. 3b).

The evolution of the crystallographic texture with increasing radius (strain) is presented for a radial section of PT0718 in Fig. 6. In the center of the sample, the fabric was produced during the earlier extension experiment with [100] axes dominantly in a vertical orientation. The section likely does not precisely intersect the center of the sample, because of difficulties in sectioning a sample exactly through its center and in assessing if exactly half a cylinder is left after sectioning. This may explain the difference in orientation between [100] maxima and [010] girdles in PT0718 relative to those in samples prior to extension tests (Fig. 5). With increasing radius and, therefore, increasing shear strain, the average [100] orientation gradually approaches the shear direction. In detail, a new maximum in [100] appears near the shear direction and strengthens as the original point maxima weakens. Thus, two [100] point maxima can be observed at shear strains near 1, a phenomenon previously observed at similar shear strains in direct shear experiments on San Carlos olivine (Zhang and Karato, 1995) and in numerical simulations of olivine texture development (Kaminski and Ribe, 2001). A corresponding rotation in the [010] girdle is observed, which, after a shear strain of ~5, begins to transform into point maxima in a manner similar to the evolution documented by Hansen et al. (2014).

The evolution of grain size, crystallographic texture strength, and texture orientation are quantified as a function of normalized radius (a proxy for strain) in Fig. 7. Grain size decreases with increasing radius. For much of its radius, the sample has reached a shear strain large enough for the microstructure to reach a steady state. The decrease in grain size as a function of radius is consistent with the change in shear stress as a function of radius in conjunction with the piezometric relationship between recrystallized grain size and stress (Karato et al., 1980; Van der Wal et al., 1993; Hansen et al., 2012c). The texture strength characterized by the M-index increases as a function of shear strain in a similar fashion to that observed in previous torsion experiments on olivine

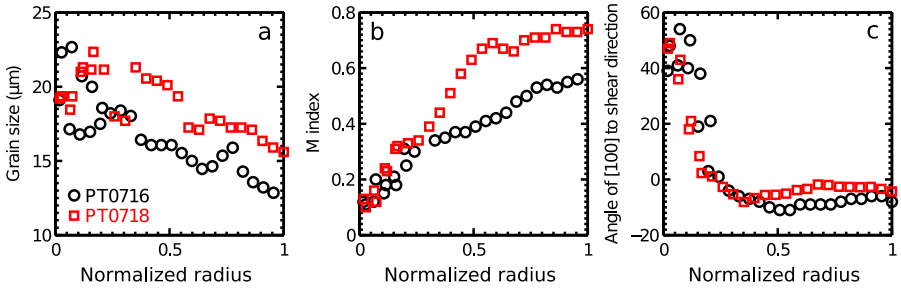

Fig. 7. (a) Grain size, (b) M index, and (c) orientation of the average [100] orientation as a function of radius for axial sections of solid cylinders deformed in torsion. Microstructures were measured within a 200 μm square sliding window. The average [100] orientation used to construct part (c) is given by the largest eigenvector of the orientation tensor describing the distribution of [100] orientations (Woodcock, 1977).

(Bystricky et al., 2000; Hansen et al., 2014). The angle between the average [100] direction and the shear direction gradually decreases to near zero at a shear strain of ∼2, a higher value of shear strain than observed in previous experiments (Zhang and Karato, 1995; Bystricky et al., 2000; Zhang et al., 2000) but similar to that documented for natural shear zones (for a review, see Skemer and Hansen, 2016) (for a review, see Skemer and Hansen, in revision).

3.2. Mechanical results

Mechanical data from extension experiments are presented in Fig. 4a and Table 2. After initial loading, both extension experiments exhibited a decrease in the apparent stress by ∼50 MPa. The stresses present in Fig. 4a are calculated assuming the volume of the sample is constant during the deformation and the diameter is uniform. However, as observed in Fig. 2, both samples thinned in a non-uniform manner such that the stress is not the same along the length of the sample throughout most of the experiment. Thus, data collected from high strain (>14%) portions of the experiment need to be corrected to take into account the non-uniform thinning. These corrected values are reported in Table 1. Stresses measured at low strain (<14%) in both samples and the sensitivity of stress to changes in strain rate observed in PT0715 agree well with the values measured in previous compression and torsion experiments on aggregates of Fo_{50} olivine without a pre-existing texture (Zhao et al., 2009; Hansen et al., 2012c). Non-uniform thinning of the sample leading to stress concentrations does not account for the total apparent stress reduction observed; nor can the stress reduction be explained by cavitation, as none was observed. Thus, the mechanical data demonstrate that the change in microstructure in extension tests affects the viscosity of the sample.

Mechanical data from torsion tests are presented in Fig. 4b and Table 2. Peak stresses just after initial loading are larger than those measured in previous compression and torsion experiments on aggregates of Fo_{50} olivine without a crystallographic texture (Zhao et al., 2009; Hansen et al., 2012c), indicating that textures developed in extension led to strengthening in torsion. At the end of our torsion experiments, the measured stresses are in good agreement with those at the end of torsion experiments on aggregates of Fo_{50} olivine without a pre-existing texture (Hansen et al., 2012c), indicating that samples deformed in torsion to sufficiently high strain evolve to a characteristic viscosity regardless of the strain history. Note that deformation of sample PT0751 does not exhibit a distinct peak stress; instead deformation occurs at a relatively constant stress of similar magnitude to that measured at high strains in other torsion experiments. This unique behavior is discussed further at the end of Section 4.1.

4. Discussion

The results presented above provide insight into two coupled phenomena, the textural evolution of olivine aggregates under changing kinematic conditions and the magnitude of viscous anisotropy at various points throughout that evolution. Here we discuss each of these phenomena, with the goal of developing a constitutive model that can be incorporated into large-scale geodynamic models.

4.1. Textural evolution

The development of crystallographic textures in olivine is of central importance in using seismic anisotropy to constrain large-scale flow patterns in the upper mantle (e.g., Hess, 1964; Tanimoto and Anderson, 1984; Becker et al., 2008, 2014; Zietlow et al., 2014). While early studies focused on olivine textures formed in triaxial compression (e.g., Ave'lallemant and Carter, 1970), a major advance in studying textural evolution came with large strain experiments carried out in simple shear, both direct shear (Zhang and Karato, 1995; Zhang et al., 2000) and torsion (Bystricky et al., 2000). These experimental milestones were accompanied by increasingly sophisticated numerical simulations of olivine textural evolution calibrated against laboratory data (Tommasi et al., 2000; Kaminski and Ribe, 2001).

Only recently have experimental investigations targeted textural evolution under changing kinematic conditions. Boneh and Skemer (2014) conducted compression experiments on cylinders of Åheim dunite with a pre-existing texture. The textural evolution varied dramatically as a function of the orientation of the pre-existing texture relative to the compression axis and developed differently than in experiments on samples without a pre-existing texture. Although the experiments of Boneh and Skemer (2014) highlight the important role of a pre-existing texture, their experimental design is limited to relatively small strains.

To complement previous data sets, the textural data presented here records the full evolution of textures formed in extension and the steady-state texture formed in torsion (Fig. 6). The strength, shape, and orientation of the textures observed at the end of high-strain torsion experiments on aggregates of olivine without a preferred crystallographic fabric (Hansen et al., 2014) are statistically indistinguishable from those formed in the torsion experiments presented here. We therefore hypothesize that, had the experiments of Boneh and Skemer (2014) been carried out to high enough strain, the textures in their samples would have reached a consistent state regardless of the initial orientation of the fabric. That said, the orientation of the texture qualitatively appears to evolve more slowly compared to aggregates without a pre-existing texture, requiring a shear strain of ∼2 for the average [100] orientation to align with the shear direction (Fig. 6). Previous experi-

Table 2
Mechanical data from extension experiments and torsion experiments.

Sample	Strain[a]	Strain rate (10^{-4} s^{-1})[b]	Stress (MPa)[b]	Grain size (μm)
Extension				
Low-strain data				
PT0715	0.07	0.528	115.1	26.6[c]
	0.08	0.258	101.1	26.6[c]
	0.11	0.505	114.0	26.6[c]
	0.12	0.746	121.7	26.6[c]
	0.14	0.492	115.2	26.6[c]
High-strain data				
PT0715a	0.46	0.627	86.5	18.3[d]
PT0715b	0.82	2.356	124.0	14.9[d]
PT071Sc	0.78	1.911	119.2	14.0[d]
PT0715d	0.34	0.439	76.8	22.1[d]
PT0715 average	0.39	0.492	62.3	–
Low-strain data				
PT0750	0.07	1.01	143	27.2[c]
High-strain data				
PT0750a	0.82	2.897	131.6	20.3[d]
PT0750b	0.88	3.844	139.7	21.3[d]
PT0750c	0.75	2.268	122.7	21.5[d]
PT0750 average	0.56	1.010	101.1	–
Torsion[e]				
PT0716	0.5	2.87	221	14.5[c]
	1.3	5.78	263	14.5[c]
	1.3	2.87	220	14.5[c]
	1.4	1.39	182	14.5[c]
	7.8	2.94	124	12.9[d]
	7.9	5.88	150	12.9[d]
	8.0	2.95	128	12.9[d]
	8.1	1.44	108	12.9[d]
	8.2	3.00	133	12.9[d]
PT0718	0.4	2.70	227	18.0[c]
	10.1	2.96	126	15.6[d]
PT0751	0.3	5.12	184	20.3[c]
	15.5	5.09	162	14.6[d]
PT0752	0.5	3.90	287	21.3[c]
	7.2	3.92	150	14.3[d]
PT0754	0.2	3.44	221	21.5[c]
	5.5	3.41	153	20.4[d]

[a] Reported values are true strain for extension experiments and shear strain for torsion experiments.
[b] For low-strain and average data, values calculated assuming homogeneous deformation. For high-strain data, values calculated using the local diameter of the sample. All values reported as equivalent (Von Mises) values.
[c] Values assumed to be that of the starting material.
[d] Values assumed to be that of the final material.
[e] Staring materials for torsion experiments are as follows: PT0715b and PT0715c for PT0716, PT0715c and PT0715d for PT0718, PT0750a for PT0751, PT0750b for PT0752, PT0750c for PT0754.

mental and field data suggest that a shear strain of ∼1 is required to align [100] axes in aggregates lacking a pre-existing texture (for a review, see Skemer and Hansen, 2016). The delay resulting from the pre-existing fabric is qualitatively in agreement with the findings of Boneh and Skemer (2014) and holds significance for interpretations of seismic anisotropy in regions of complex kinematics. However, the magnitude of this delay is less than observed for naturally deformed samples for which [100] does not align with the shear direction until shear strains >3 (for a review, see Skemer and Hansen, 2016). The relative rates of textural evolution in different experimental scenarios are compared quantitatively in Part 2 of this series.

Dynamic recrystallization appears to play an important role in the textural evolution at low strain. As observed in Fig. 6, [100] axes exhibit a near vertical point maximum at low strain in the torsion experiment due to the earlier fabric developed in extension. By a shear strain of 0.7, a second weak maximum appears subparallel to the flow direction. Zhang et al. (2000) observed a similar double maximum in direct shear experiments, which they attributed to the activation of multiple slip systems. However, Lee et al. (2002) subsequently suggested that preferential growth of grains unfavorably orientated for slip on (010)[100] produces the [100] maximum at a high angle to the shear direction. Both of these hypotheses assume that the two point maxima represent the steady-state texture. In contrast, our results demonstrate that the presence of two peaks is a transient phenomenon, and because the second point maximum strengthens at the expense of the first as the shear strain approaches 2, we suggest that the presence of a double maximum is not primarily the result of the activation of two slip systems. If the nucleation of new grains in a soft orientation is an important mechanism, it might lead to enhanced rates of textural evolution, a phenomenon incorporated into DREX by Kaminski and Ribe (2001). If the rate of dynamic recrystallization is decreased at lower temperatures, then textural evolution in aggregates with a pre-existing fabric could be increasingly delayed. Indeed, Zhang et al. (2000) observed a slower evolution of the texture orientation in experiments conducted at 1473 K relative to those conducted at 1573 K.

Another noteworthy aspect of our results is the girdles formed in distributions of the [100], [010], and [001] axes in our extension experiments (Fig. 5). To our knowledge, olivine textures formed in extension experiments have not previously been investigated in a rheological regime in which intracrystalline plasticity is important (compare with Miyazaki et al., 2013). Knoll et al. (2009), however, did predict strong point maxima for [100] axes rather than girdles in their numerical simulations of textural evolution in extension. The striking difference between our observations and the simulations indicates that some of the underlying microphysical phenomena occurring in our experiments, such as grain-boundary sliding and dynamic recrystallization, modify the textural evolution in a manner not fully captured in simulations that only involve dislocation glide.

One sample deformed in extension (PT0750a) did not exhibit the girdles described above but instead exhibiting point maxima for all three crystallographic axes (Fig. 5). We suggest that these point maxima are related to local necking of the sample during extension that promoted simple shear over coaxial deformation, preferentially activating (001)[100] and (100)[001] slip due to the initial orientation of the girdles. This sample therefore had a unique texture at the start of the subsequent torsion test (PT0751), which may have led to the decreased stress at low strains in PT0751 relative to other torsion experiments (Fig. 4b).

4.2. Magnitude of anisotropy

This study (extension then torsion) and Hansen et al. (2012a) (torsion then extension) represent a complimentary set of experiments and form the basis for the analysis below. We compare the mechanical data from these datasets in Fig. 8. To facilitate this comparison, we use the equivalent (or von Mises) stress, defined as $\sqrt{3J}$, where J is the second invariant of the deviatoric stress tensor. The equivalent stress allows comparison of data obtained from samples deformed under complicated stress states with different signs and/or symmetries. Stresses measured in samples without a pre-existing fabric deformed in extension (black data points, this study) are comparable to those measured in compression tests (black line, Zhao et al., 2009; Hansen et al., 2012c), indicating that the mechanical response of these samples is isotropic. We group the data from textured samples into data from those samples for which the orientation of anisotropy has a weakening effect (red data) and data from those samples for which the orientation has a strengthening effect (blue). This grouping illustrates that the presence of a crystallographic texture can change the viscosity by approximately an order of magnitude, depending on the orientation of the principle stresses relative to the texture.

Various methods exist for parameterizing viscous anisotropy, either as a scalar (e.g., Lev and Hager, 2008, 2011) or a tensor (e.g., Becker and Kawakatsu, 2011). In this first of two papers on viscous anisotropy, we seek a scalar variable to describe the magnitude of anisotropy. We previously defined the magnitude of anisotropy as the ratio of the viscosity measured in extension to the viscosity measured in torsion (Hansen et al., 2012a). Because the present study explores a different strain path than our previous work, we adopt a more general terminology here that accounts for the orientation of the texture relative to the principal stresses. We define the magnitude of anisotropy as the ratio of the viscosity measured in the strong orientation relative to the viscosity measured in the weak orientation,

$$\delta = \left(\frac{\dot{\varepsilon}_{e,w}}{\dot{\varepsilon}_{e,s}}\right)\left(\frac{\sigma_{e,s}}{\sigma_{e,w}}\right)^n, \tag{2}$$

where $\dot{\varepsilon}$ is the strain rate, σ is the stress, n is the stress exponent, the subscript e indicates the von Mises equivalent value, and the subscripts w and s indicate the values measured in the weak and strong orientations, respectively. If we consider the anisotropy at conditions of constant stress, then the magnitude of anisotropy is entirely defined by the ratio of strain rate measured in a weak orientation to that in a strong orientation. In our previous work, $\dot{\varepsilon}_{e,w}$ corresponds to values measured in torsion experiments and $\dot{\varepsilon}_{e,s}$ corresponds to values measured in extension experiments (Hansen et al., 2012a). Because of the reversed strain path and different texture orientation in the present study, $\dot{\varepsilon}_{e,w}$ corresponds here to values measured in extension experiments, and $\dot{\varepsilon}_{e,s}$ corresponds to values measured in torsion experiments.

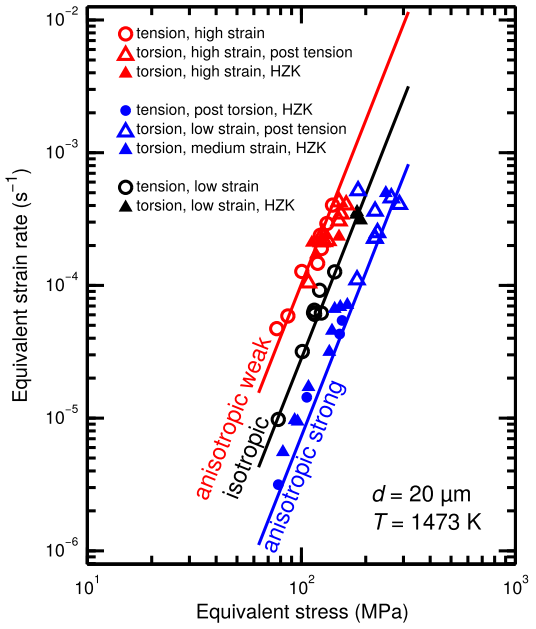

Fig. 8. Equivalent (von Mises) strain rate as a function of equivalent (von Mises) stress for the entire data set. Open symbols are data from this study and closed symbols are data from Hansen et al. (2012a) (HZK). Black symbols indicate data obtained from experiments on samples without a pre-existing texture. Blue symbols indicate data obtained from experiments on samples with a strong texture and anisotropic viscosity deformed in a strong orientation. Red symbols indicate data obtained from experiments on samples with a strong texture and anisotropic viscosity deformed in a weak orientation. Solid lines indicate predictions from the model of Hansen et al. (2012a) for isotropic, strong ($F = 1.39$) and weak ($F = 0.73$) cases. All data are normalized to constant grain size using a grain size exponent of $p = 0.73$ from Hansen et al. (2011, 2012c). (For interpretation of the references to color in this figure legend, the reader is referred to the web version of this article.)

We have also previously described the effect of anisotropy on strain rate using the relationship

$$\dot{\varepsilon} = A\left(\frac{\sigma}{F}\right)^n, \tag{3}$$

where A is a scalar that depends on the grain size and temperature and F describes the effect of the texture on strain rate. Thus, δ can be alternatively given by

$$\delta = \left(\frac{F_s}{F_w}\right)^n. \tag{4}$$

We previously determined F to have a value of $F_w = 0.73$ for samples that weakened during deformation to high strain in torsion (Hansen et al., 2012c) and a value of $F_s = 1.39$ for samples deformed in extension after being deformed to high strain in torsion (Hansen et al., 2012a). We also determined a value for the stress exponent of $n = 4.1$ (Hansen et al., 2012c). Stress-strain rate relationships calculated using these values for F, which are presented as red and blue lines in Fig. 8, demonstrate good agreement between data from our previous work and the new data presented here. These values of F suggest that the stress measured at the

beginning of a torsion experiment would be about a factor of 2 larger than the stress measured at the end of the tension experiment, consistent with the mechanical data if differences in strain rate and grain size are taken into account.

The simple parameterization given by equation (3) can be used to predict the viscous anisotropy of a given aggregate. We calculate values of δ of $\sim$14 for the above values of F, indicating that viscosity can differ by an order of magnitude depending on the orientation of the principle stresses relative to the texture. However, predicting the mechanical response in more complicated stress states and the evolution of anisotropy throughout complex strain paths still requires a more sophisticated micromechanical model. Calibration of a mechanical and textural evolution model with this dataset is the focus of Part 2.

There are two main caveats to consider in applying our results to deformation in natural systems at geological conditions. First, the rheological behavior of the high-iron-content olivine investigated in this study (Fo_{50}) and the more magnesium-rich olivine typical of upper-mantle rocks ($\sim Fo_{90}$) is different, primarily due to the lower viscosity and larger stress exponent in the high-iron content material (Zhao et al., 2009). These differences do not markedly influence the magnitude of viscous anisotropy because (1) iron content does not dramatically affect the relative strengths of different slip systems (Kohlstedt and Ricoult, 1984) and (2) the textural evolution is statistically indistinguishable between aggregates of Fo_{50} and those of San Carlos olivine (Fo_{90}) (Hansen et al., 2014). We suggest that, although values for A and n are different for iron-poor samples, values for F presented here can be applied to olivines of all ferromagnesian compositions.

The second caveat is that the scalar measure of anisotropy presented here is limited to a specific set of kinematic conditions. Notably, the formulation of δ assumes that the material has transverse isotropy (i.e., hexagonal symmetry) with the axis of isotropy parallel to the torsion and extension axes. The observed textures, however, clearly exhibit lower symmetry; thus, viscous anisotropy will also exhibit lower symmetry. Fully characterizing the anisotropy requires a 4th-rank tensor with 21 unknown parameters. Effects related to this lower symmetry will be important in situations in which flow is 3 dimensional, potentially with evolving kinematics. Thus, an ideal constitutive model would (1) capture the subtleties of the textural evolution in an arbitrary deformation in which the kinematics might be changing and (2) provide a description of the anisotropy that resolves a viscosity with arbitrary symmetry. The second paper in this series will develop a constitutive model that captures the textural evolution and mechanical anisotropy under these more general conditions.

5. Conclusion

We conducted a series of laboratory experiments on synthetic aggregates of Fo_{50} olivine in gas-medium apparatus to determine the viscous anisotropy in textured aggregates of olivine. In a reverse order relative to previous experiments, we performed extension experiments followed by torsion experiments.

Extension experiments yielded samples with a unique crystallographic texture defined by small circles of [100] axes at $\sim$40° to the extension axis. Subsequent torsion experiments yielded samples with similar textures to previous high-strain torsion experiments, indicating that textures evolve to a consistent steady-state independent of any pre-existing fabric. Radial transects of torsion samples reveal the full history of textural evolution during the torsion tests, providing a data set that can be used to calibrate textural evolution models in future studies.

Mechanical data demonstrate pronounced weakening during extension that we attribute to formation of a preferred crystallographic texture. Torsion experiments also indicate weakening during deformation. The textures formed in extension yield anisotropic viscosities of a similar magnitude to those in our prior work (Hansen et al., 2012a). Our results establish that the magnitude of anisotropy can be large and primarily dependent on the strength, rather than the shape, of the crystallographic texture. Thus, at least for simple stress states, the anisotropy in viscosity can be reasonably parameterized as a scalar. The experiments presented here provide a key data set for calibrating future micromechanical models that will allow anisotropic mechanical behavior to be determined for general stress states and complicated strain paths.

Acknowledgements

This work benefitted greatly from discussions with Manuele Faccenda and Shun Karato. The manuscript was significantly improved by thoughtful comments from Georg Dresen and Andréa Tommasi. K. Barton and the Department of Plant Biology, Carnegie Institution, are thanked for SEM access. This research was supported by funding awards including John Fell Fund, University of Oxford 123/718 and NERC NE/M000966/1 to LNH, NSF EAR-1255620 to JMW, and NSF EAR-1214876 to DLK.

Appendix A. Supplementary material

Supplementary material related to this article can be found online at http://dx.doi.org/10.1016/j.epsl.2016.04.008.

References

Ave'lallemant, H.G., Carter, N.L., 1970. Syntectonic recrystallization of olivine and modes of flow in the upper mantle. Geol. Soc. Am. Bull. 81 (8), 2203–2220. http://dx.doi.org/10.1130/0016-7606(1970)81[2203:SROOAM]2.0.CO;2.

Bachmann, F., Hielscher, R., Schaeben, H., 2010. Texture analysis with MTEX – free and open source software toolbox. Diffus. Defect Data Solid State Data, Pt. B Solid State Phenom. 160, 63–68.

Bai, Q., Mackwell, S., Kohlstedt, D., 1991. High-temperature creep of olivine single crystals, 1: mechanical results for buffered samples. J. Geophys. Res., Solid Earth 96 (B2), 2441–2463.

Becker, T.W., Kawakatsu, H., 2011. On the role of anisotropic viscosity for plate-scale flow. Geophys. Res. Lett. 38 (17), L17307. http://dx.doi.org/10.1029/2011GL048584.

Becker, T.W., Kustowski, B., Ekström, G., 2008. Radial seismic anisotropy as a constraint for upper mantle rheology. Earth Planet. Sci. Lett. 267 (1–2), 213–227. http://dx.doi.org/10.1016/j.epsl.2007.11.038.

Becker, T.W., Conrad, C.P., Schaeffer, A.J., Lebedev, S., 2014. Origin of azimuthal seismic anisotropy in oceanic plates and mantle. Earth Planet. Sci. Lett. 401, 236–250. http://dx.doi.org/10.1016/j.epsl.2014.06.014.

Bercovici, D., Ricard, Y., Richards, M.A., 2000. The relation between mantle dynamics and plate tectonics: a primer. In: Richards, M., Gordon, R., van der Hilst, R. (Eds.), The History and Dynamics of Global Plate Motions, vol. 121. AGU, Washington, D.C., pp. 5–46.

Boneh, Y., Skemer, P., 2014. The effect of deformation history on the evolution of olivine CPO. Earth Planet. Sci. Lett. 406, 213–222.

Bystricky, M., Kunze, K., Burlini, L., Burg, J.-P., 2000. High shear strain of olivine aggregates: rheological and seismic consequences. Science 290 (5496), 1564–1567. http://dx.doi.org/10.1126/science.290.5496.1564.

Castelnau, O., Blackman, D.K., Becker, T.W., 2009. Numerical simulations of texture development and associated rheological anisotropy in regions of complex mantle flow. Geophys. Res. Lett. 36 (12), L12304. http://dx.doi.org/10.1029/2009GL038027.

Christensen, U.R., 1987. Some geodynamical effects of anisotropic viscosity. Geophys. J. R. Astron. Soc. 91 (3), 711–736. http://dx.doi.org/10.1111/j.1365-246X.1987.tb01666.x.

Durham, W.B., Goetze, C., Blake, B., 1977. Plastic flow of oriented single crystals of olivine, 2: observations and interpretations of the dislocation structures. J. Geophys. Res. 82 (36), 5755–5770. http://dx.doi.org/10.1029/JB082i036p05755.

Freed, A.M., Hirth, G., Behn, M.D., 2012. Using short-term postseismic displacements to infer the ambient deformation conditions of the upper mantle. J. Geophys. Res. 117 (B1). http://dx.doi.org/10.1029/2011JB008562.

Han, D., Wahr, J., 1997. An analysis of anisotropic mantle viscosity, and its possible effects on post-glacial rebound. Phys. Earth Planet. Inter. 102 (1), 33–50. http://dx.doi.org/10.1016/S0031-9201(96)03268-2.

Hansen, L.N., Zimmerman, M.E., Kohlstedt, D.L., 2011. Grain boundary sliding in San Carlos olivine: flow law parameters and crystallographic-preferred orientation. J. Geophys. Res., Solid Earth 116 (B8), B08201. http://dx.doi.org/10.1029/2011JB008220.

Hansen, L.N., Zimmerman, M.E., Kohlstedt, D.L., 2012a. Laboratory investigations of the viscous anisotropy of olivine aggregates. Nature 492, 415–418. http://dx.doi.org/10.1038/nature11671.

Hansen, L.N., Dillman, A.M., Zimmerman, M.E., Kohlstedt, D.L., 2012b. Strain localization in olivine aggregates at high temperature: an experimental comparison of constant-strain-rate and constant-stress boundary conditions. Earth Planet. Sci. Lett. 333–334, 134–145. http://dx.doi.org/10.1016/j.epsl.2012.04.016.

Hansen, L.N., Zimmerman, M.E., Kohlstedt, D.L., 2012c. The influence of microstructure on deformation of olivine in the grain-boundary sliding regime. J. Geophys. Res. 117, B09201. http://dx.doi.org/10.1029/2012JB009305.

Hansen, L.N., Zhao, Y.-H., Zimmerman, M.E., Kohlstedt, D.L., 2014. Protracted fabric evolution in olivine: implications for the relationship among strain, crystallographic fabric, and seismic anisotropy. Earth Planet. Sci. Lett. 387, 157–168. http://dx.doi.org/10.1016/j.epsl.2013.11.009.

Hearn, E.H., Humphreys, E.D., Chai, M., Brown, J.M., 1997. Effect of anisotropy on oceanic upper mantle temperatures, structure, and dynamics. J. Geophys. Res., Solid Earth 102 (B6), 11943–11956. http://dx.doi.org/10.1029/97JB00506.

Heilbronner, R.P., 1992. The autocorrelation function: an image processing tool for fabric analysis. Tectonophysics 212 (3–4), 351–370. http://dx.doi.org/10.1016/0040-1951(92)90300-U.

Hess, H.H., 1964. Seismic anisotropy of the uppermost mantle under oceans. Nature 203 (4945), 629–631. http://dx.doi.org/10.1038/203629a0.

Hirth, G., Kohlstedt, D.L., 1995. Experimental constraints on the dynamics of the partially molten upper mantle, 1: deformation in the diffusion creep regime. J. Geophys. Res. 100, 1981–2001. http://dx.doi.org/10.1029/94JB02128.

Kaminski, E., Ribe, N., 2001. A kinematic model for recrystallization and texture development in olivine polycrystals. Earth Planet. Sci. Lett. 189 (3–4), 253–267. http://dx.doi.org/10.1016/S0012-821X(01)00356-9.

Karato, S., Toriumi, M., Fujii, T., 1980. Dynamic recrystallization of olivine single crystals during high-temperature creep. Geophys. Res. Lett. 7 (9), 649–652.

Keefner, J.W., Mackwell, S.J., Kohlstedt, D.L., Heidelbach, F., 2011. Dependence of dislocation creep of dunite on oxygen fugacity: implications for viscosity variations in Earth's mantle. J. Geophys. Res. 116 (B5), B05201. http://dx.doi.org/10.1029/2010JB007748.

Knoll, M., Tommasi, A., Logé, R.E., Signorelli, J.W., 2009. A multiscale approach to model the anisotropic deformation of lithospheric plates. Geochem. Geophys. Geosyst. 10, Q08009. http://dx.doi.org/10.1029/2009GC002423.

Kohlstedt, D.L., Ricoult, D.L., 1984. High-temperature creep of silicate olivines. In: Tressler, R.E., Bradt, R.C. (Eds.), Deformation of Ceramic Materials II. Springer, US, pp. 251–280.

Lee, K.-H., Jiang, Z., Karato, S., 2002. A scanning electron microscope study of the effects of dynamic recrystallization on lattice preferred orientation in olivine. Tectonophysics 351 (4), 331–341. http://dx.doi.org/10.1016/S0040-1951(02)00250-0.

Lenardic, A., Moresi, L.-N., Mühlhaus, H., 2003. Longevity and stability of cratonic lithosphere: insights from numerical simulations of coupled mantle convection and continental tectonics. J. Geophys. Res., Solid Earth 108 (B6), 2303. http://dx.doi.org/10.1029/2002JB001859.

Lev, E., Hager, B.H., 2008. Rayleigh–Taylor instabilities with anisotropic lithospheric viscosity. Geophys. J. Int. 173 (3), 806–814. http://dx.doi.org/10.1111/j.1365-246X.2008.03731.x.

Lev, E., Hager, B.H., 2011. Anisotropic viscosity changes subduction zone thermal structure. Geochem. Geophys. Geosyst. 12 (4).

Mei, S., Kohlstedt, D.L., 2000. Influence of water on plastic deformation of olivine aggregates, 1: diffusion creep regime. J. Geophys. Res. 105 (B9), 21457–21469. http://dx.doi.org/10.1029/2000JB900179.

Michibayashi, K., Mainprice, D., 2004. The role of pre-existing mechanical anisotropy on shear zone development within oceanic mantle lithosphere; an example from the Oman Ophiolite; orogenic lherzolites and mantle processes. J. Petrol. 45 (2), 405–414.

Mitrovica, J.X., Forte, A.M., 2004. A new inference of mantle viscosity based upon joint inversion of convection and glacial isostatic adjustment data. Earth Planet. Sci. Lett. 225 (1–2), 177–189. http://dx.doi.org/10.1016/j.epsl.2004.06.005.

Miyazaki, T., Sueyoshi, K., Hiraga, T., 2013. Olivine crystals align during diffusion creep of Earth/'s upper mantle. Nature 502 (7471), 321–326. http://dx.doi.org/10.1038/nature12570.

Paterson, M.S., 1990. Rock deformation experimentation. In: Duba, A.G., Durham, W.B., Handin, J.W., Wang, H.F. (Eds.), The Brittle Ductile Transition in Rocks, The Heard Volume, vol. 56. AGU, Washington, D.C., pp. 187–194.

Paterson, M.S., Olgaard, D.L., 2000. Rock deformation tests to large shear strains in torsion. J. Struct. Geol. 22 (9), 1341–1358. http://dx.doi.org/10.1016/S0191-8141(00)00042-0.

Raterron, P., Girard, J., Chen, J., 2012. Activities of olivine slip systems in the upper mantle. Phys. Earth Planet. Inter.

Skemer, P., Hansen, L.N., 2016. Inferring mantle flow from seismic anisotropy: an experimental perspective. Tectonophysics 668–669, 1–14. http://dx.doi.org/10.1016/j.tecto.2015.12.003.

Skemer, P., Warren, J.M., Hansen, L.N., Hirth, G., Kelemen, P.B., 2013. The influence of water and LPO on the initiation and evolution of mantle shear zones. Earth Planet. Sci. Lett.

Tackley, P.J., 2000. The quest for self-consistent generation of plate tectonics in mantle convection models. In: Richards, M., Gordon, R., van der Hilst, R. (Eds.), The History and Dynamics of Global Plate Motions, vol. 121. AGU, Washington, D.C., pp. 47–72.

Tanimoto, T., Anderson, D.L., 1984. Mapping convection in the mantle. Geophys. Res. Lett. 11 (4), 287–290. http://dx.doi.org/10.1029/GL011i004p00287.

Tommasi, A., Mainprice, D., Canova, G., Chastel, Y., 2000. Viscoplastic self-consistent and equilibrium-based modeling of olivine lattice preferred orientations: implications for the upper mantle seismic anisotropy. J. Geophys. Res. 105, 7893–7908. http://dx.doi.org/10.1029/1999JB900411.

Tommasi, A., Knoll, M., Vauchez, A., Signorelli, J.W., Thoraval, C., Logé, R., 2009. Structural reactivation in plate tectonics controlled by olivine crystal anisotropy. Nat. Geosci. 2 (6), 423–427. http://dx.doi.org/10.1038/ngeo528.

Urai, J.L., Means, W.D., Lister, G.S., 1986. Dynamic recrystallization of minerals. In: Mineral and Rock Deformation: Laboratory Studies. Geophys. Monogr. Ser., vol. 36. Am. Geophys. Union, Wash., DC, pp. 161–199.

Van der Wal, D., Chopra, P., Drury, M., Gerald, J.F., 1993. Relationships between dynamically recrystallized grain size and deformation conditions in experimentally deformed olivine rocks. Geophys. Res. Lett. 20 (14), 1479–1482. http://dx.doi.org/10.1029/93GL01382.

Vauchez, A., Tommasi, A., Barruol, G., 1998. Rheological heterogeneity, mechanical anisotropy and deformation of the continental lithosphere. Tectonophysics 296 (1–2), 61–86. http://dx.doi.org/10.1016/S0040-1951(98)00137-1.

Wendt, A.S., Mainprice, D., Rutter, E., Wirth, R., 1998. A joint study of experimental deformation and experimentally induced microstructures of pretextured peridotites. J. Geophys. Res. 103 (B8), 18205–18221.

Woodcock, N.H., 1977. Specification of fabric shapes using an eigenvalue method. Geol. Soc. Am. Bull. 88 (9), 1231–1236. http://dx.doi.org/10.1130/0016-7606(1977)88<1231:SOFSUA>2.0.CO;2.

Zhang, S., Karato, S., 1995. Lattice preferred orientation of olivine aggregates deformed in simple shear. Nature 375 (6534), 774–777. http://dx.doi.org/10.1038/375774a0.

Zhang, S., Karato, S., Fitz Gerald, J., Faul, U.H., Zhou, Y., 2000. Simple shear deformation of olivine aggregates. Tectonophysics 316 (1–2), 133–152. http://dx.doi.org/10.1016/S0040-1951(99)00229-2.

Zhao, Y.H., Zimmerman, M.E., Kohlstedt, D.L., 2009. Effect of iron content on the creep behavior of olivine: 1. Anhydrous conditions. Earth Planet. Sci. Lett. 287 (1–2), 229–240. http://dx.doi.org/10.1016/j.epsl.2009.08.006.

Zietlow, D.W., Sheehan, A.F., Molnar, P.H., Savage, M.K., Hirth, G., Collins, J.A., Hager, B.H., 2014. Upper mantle seismic anisotropy at a strike-slip boundary: South Island, New Zealand. J. Geophys. Res., Solid Earth 119 (2), 1020–1040.